Materials Reports Solidwaste & Ecomaterials

Materials Reports: Solidwaste and Ecomaterials

Journal Homepage: www.sciopen.com/journal/3078-4093

Original Research Report

Preparation, performances and hydration mechanism of high-entropy solid waste-based binders

Dongmin Wang [1, *], Huangqi Wang [2, *], Peiliang Shen [3], Jixiang Wang [1], Rui Sun [1], Bo Liu [4], Moncef Nehdi [5]

[1] School of Chemical and Environmental Engineering, China University of Mining and Technology-Beijing, Beijing, 100083, China

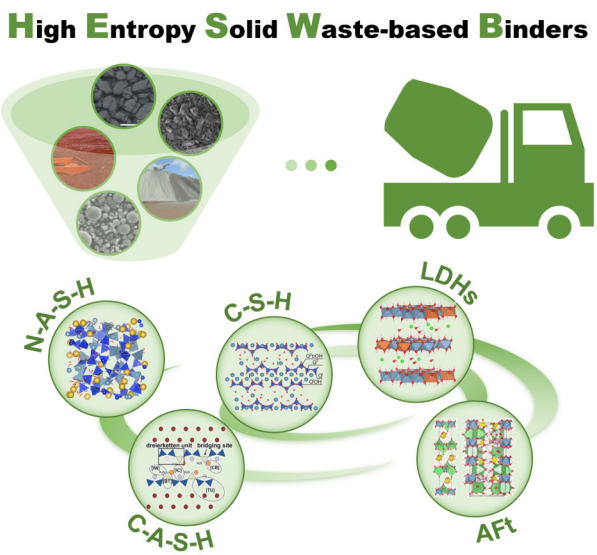
[2] Department of Civil Engineering, Tsinghua University, Beijing, 100084, China

[3] Department of Civil and Environmental Engineering, The Hong Kong Polytechnic University, Hong Kong, China

[4] School of Mechanics and Civil Engineering, China University of Mining and Technology-Beijing, Beijing, 100083, China

[5] Department of Civil Engineering, McMaster University, Hamilton, Ontario, L8S 4M6, Canada

Abstract: High-entropy materials (HEMs) are a novel class of materials characterized by the incorporation of at least five principal elements, resulting in four core effects: high-entropy, severe-lattice-distortion, sluggish-diffusion, and cocktail effects. Inspired by these principles, this study proposes the concept of a high-entropy solid waste-based binder (HESWB), synthesized from blast furnace slag (BFS), fly ash (FA), carbide slag (CS), red mud (RM), and desulfurization gypsum (DG). The roles of individual components in influencing strength development, hydration behavior, and pore structure were systematically analyzed. Compared to ordinary Portland cement (PC), HESWB-based concrete exhibited a 24% and 14% reduction in static elastic modulus for natural coarse aggregate and ceramsites, respectively, a more than 82% reduction in autogenous shrinkage, and almost no chloride penetration after 28 d. These improvements are attributed to the synergistic effects among the diverse components, which refine the pore structure and alter the hydration kinetics. This study not only introduces a sustainable approach for utilizing industrial solid wastes but also demonstrates the potential of HESWBs to enhance concrete durability and performance, offering promising implications for future cementitious systems.



Keywords: high-entropy materials, cementitious material, solid waste, concrete, durability

Citation: D. Wang, H. Wang, P. Shen, et al. Preparation, performances and hydration mechanism of high-entropy solid waste-based binders. *Materials Reports: Solidwaste and Ecomaterials*, 2025, 1: 9520015. https://doi.org/10.26599/MRSE.2025.9520015.

1. Introduction

High-entropy materials (HEMs) emerged as a field of research in 2004, when the first research on high-entropy alloys was published. The scope was soon expanded from high-entropy alloys to medium-entropy alloys, as well as ceramics[1], polymers[2], and composite materials[3]. Four core effects in HEMs are used to describe their unique fundamental performances,

*Correspondence to D. Wang, wangdongmin@cumtb.edu.cn; H. Wang, wanghuangqi1995@163.com

Received 31 March 2025; Received in revised form 21 July 2025; Accepted 24 July 2025

©2025 The Authors. Publishing services by Tsinghua University Press. This is an open access article under the CC BY license (https://creativecommons.org/licenses/by/4.0/)

which are high-entropy, severe-lattice-distortion, sluggish-diffusion, and cocktail effects[4,5]. The relative diagram is shown in Fig. 1.

▪ High -entropy effect describes an entropy driving process that elements or particles in HEMs would strongly inhibit the phase separation. More solid solutions and/or amorphous phases would be generated in HEMs instead of some coexisting crystalline phases.

▪ Severe-lattice-distortion effect shows a result of an insufficient crystallization, which is also the result of a high-entropy effect.

▪ Sluggish -diffusion effect is a kinetic equilibrium result in HEMs, where the complex microstructure would stably exist for a long time in their service environment. This microstructure is also the base of unique performances in HEMs.

▪ Cocktail effect means a mixed effect of different elements or particles in HEMs. When an unpredicted performance appears in an HEM, it is always attributed to the cocktail effect.

These four core effects originate from more than five elements or particles added in HEMs. When the contents of these elements or particles are 5% to 35%, the complex interaction among them would form some solid solutions[6–8].

Portland cement (PC) has been researched and applied for more than 200 years. PC includes C_3S, C_2S, C_3A, C_4AF, gypsum, and other mineral admixtures. It has a complex hydration reaction, but the main hydration reaction is still the hydration of C_3S and the pozzolanic reaction[9]. Researchers developed many methods to adjust these hydration processes[10–20], and the performances are basically predictable[21–27]. Using machine learning methods or other computational methods, their various performances could be designed and predicted[28–31]. However, when we want some new performances from cementitious materials, new binders are necessary. Many novel binders are developed, such as aluminate cement, sulphoaluminate cement, alkali-activated cement, various magnesium cements, and others[32,33]. All of them mainly involve only one hydration reaction, so their performances are difficult to adjust widely.

Referring to the principle of HEMs, we mixed five solid wastes, including blast furnace slag (BFS), fly ash (FA), carbide slag (CS), red mud (RM), and desulfurization gypsum (DG), to prepare a novel binder, named high-entropy solid waste-based binder (HESWB). Unlike other HEMs, HESWB is still a semi-finished product before mixing with water. Therefore, the hydration process of HESWB would present these four core effects, and these aspects are discussed in detail. First, the influence of compositions on fluidity and strength was studied. The hydration process and products were characterized. Then, the durability and volume stability of HESWB-based products were researched.

2. Materials and methods

2.1. Materials

Blast furnace slag (BFS), fly ash (FA), carbide slag (CS), red mud (RM), and desulfurization gypsum (DG) were obtained from the local industry in Henan Province, China. Their chemical compositions were measured via an energy dispersive X-ray fluorescence spectrometer (Shimadzu EDX-7000), and the loss on ignition (LOI) was tested by a muffle furnace. Both results are shown in Table 1. Portland cement (PC), natural sand, coarse aggregate (AG), and superplasticizer (SP) were from the Beijing Building Materials Academy of Scientific Research (BBMA), China. Two types of AGs were used in this study, and the performances of both products comply with the Chinese national standard of GB/T 14685—2022. The particle size ranges were 5–10 mm and 10–16 mm, marked as AG(5-10) and AG(10-16), respectively. Meanwhile, two types of ceramsites were used with particle sizes of 5–10 mm and 10–16 mm, respectively. BFS, FA, CS, RM, and DG were ground into similar fineness. Particle size distributions of them were tested by a particle size analyzer (Malvern Mastersizer 2000), and their results are shown in Fig. 2.

2.2. Preparation

2.2.1. Preparation of HESWBs

The discussion about the raw compositions included two parts. In the first part, the influence of BFS, RM, and DG on fluidity, strength, and hydration products was discussed, and the

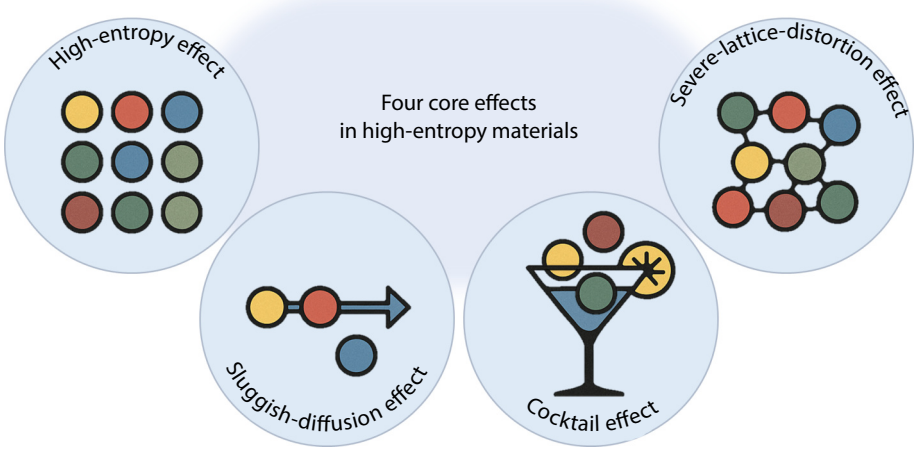


Fig. 1. Four core effects in high-entropy materials.

Table 1. Chemical compositions of raw material.

Compositions	BFS	FA	CS	RM	DG	PC
CaO	44.90	3.90	93.50	48.80	41.17	45.28
SiO_2	29.07	54.73	2.56	21.20	6.85	26.30
Al_2O_3	13.13	28.27	1.30	6.44	2.27	11.83
MgO	8.27	0.73	0.16	1.50	4.08	6.28
SO_3	1.53	1.10	0.76	0.83	42.36	2.67
TiO_2	0.89	1.43	0.05	3.84	0.13	4.56
MnO	0.64	0.05	0.01	0.05	0.02	0.54
K_2O	0.43	2.24	0.00	0.99	0.48	0.48
Fe_2O_3	0.43	5.97	0.40	11.57	0.89	0.86
others	0.72	1.58	1.27	4.78	1.75	1.20
LOI	3.1	5.2	29.44	29.00	3.09	3.05

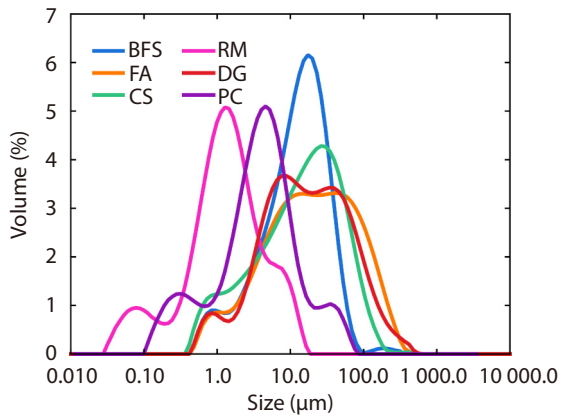


Fig. 2. Particle size distributions of raw materials.

compositions of these raw materials are shown in Fig. 3. In this part, the HESWBs contained 20 wt% FA and no CS. In the second part, the roles of FA, RM, and CS were researched separately, and the markers of the samples were listed in Table 2. To focus on the influence of variables and shorten the length of the markers, the sample with the same compositions would use different markers in different sections, like FA30, RM10, and CS2.0.

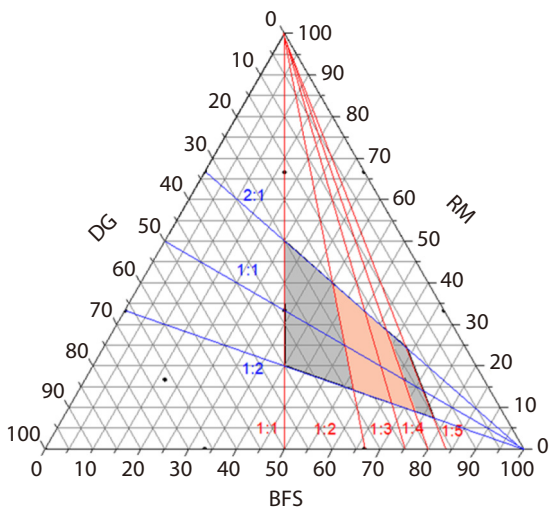


Fig. 3. Compositions of raw materials with 20 wt% FA and without CS.

Table 2. Compositions of raw materials in HESWBs (wt%).

Markers	BFS	FA	DG	RM	CS
FA0	78	0	10	10	2
FA20	58	20	10	10	2
FA30	48	30	10	10	2
FA40	38	40	10	10	2
RM0	58	30	10	0	2
RM10	48	30	10	10	2
RM20	38	30	10	20	2
RM30	28	30	10	30	2
CS0.5	49.5	30	10	10	0.5
CS1.0	49	30	10	10	1
CS1.5	48.5	30	10	10	1.5
CS2.0	48	30	10	10	2
CS3.0	47	30	10	10	3

2.2.2. Preparation of HESWB-based concrete

To compare the differences between HESWB and PC on the performances of concretes, two types of aggregates were used to prepare concretes, marked as N and A to represent natural and artificial aggregates, respectively. The mixing design of concrete is listed in Table 3. All raw materials including water, were put into a horizontal mixer and mixed for 10 min. Then, mortars were molded into prisms with a size of 100 mm × 100 mm × 100 mm, and cured in water until the required ages of 1, 7, and 28 d. Then, the strength of mortars was tested by a universal testing machine (INSTRON 6025). During the testing process, the loading rate was 0.6 MPa s^{-1}.

Table 3. Mixing design of concrete (kg).

Concrete	PC/HESWB	Sand	AG(5-10)	AG(10-16)	SP	Water
PC_N	420.0	787.8	671.3	447.5	1.05	146.6
PC_A	420.0	787.8	486.7	325.0	1.05	146.6
HESWB_N	386.8	787.8	671.3	447.5	2.10	146.4
HESWB_A	386.8	787.8	486.7	325.0	2.10	146.4

2.3. Fluidity and strength testing

The contents of HESWBs, standard sand, and water in testing mortars were 450, 1350, and 225 g, respectively. Mortars were mixed well and then tested for fluidity and strength. The mixing procedure of mortars was as follows. HESWBs and water were added into a planetary mixer and mixed for 30 s at 80 rpm; then standard sand was added with mixing at 80 rpm. After that, the mortar was mixed at 240 rpm for 30 s, stopped for 90 s, and mixed at 240 rpm for 90 s. For the fluidity, fresh mortars were placed into a conical mold on a flow table. Lift the mold and allow the mortar to spread freely. Then, drop the flow table 25 times within 15 s, and measure the diameter of the spread mortar in two perpendicular directions. The average of these measurements was recorded as the flow value, expressed as a percentage of the original diameter. Following this, mortars were molded into prisms with a size of 40 mm × 40 mm × 160 mm, and cured in water until the required ages of 1, 7, and 28 d. Then, the strength of mortars was tested by a universal testing

machine (INSTRON 6025). During the testing process, the loading rate was 2.4 kN s^{-1}.

2.4. Static elastic modulus testing

The testing samples were the same as those for strength testing, and their preparation can be seen in Section 2.3. A universal testing machine (INSTRON 6025) was used to test the static elastic modulus, and the testing program is shown in Fig. 4b.

2.5. Shrinkage testing

The preparation method of concrete was the same as that in Section 2.2.2. The concrete autogenous shrinkage test was conducted using the setup shown in Fig. 5a[34,35]. A PTFE layer approximately 3 mm thick was applied inside the mold. After pouring the concrete, the mold was coated with a PE film to reduce water loss from the concrete. Then, the LVDT was connected with the specimens. After filling the mold with the fresh concrete mixture, the PE film was immediately applied and sealed. After the concrete had set (approximately 12 h after pouring), the surrounding PTFE layer was carefully removed, and the LVDT was adjusted to the correct position to begin recording data. After completing the measurements, the thin rod connected to the LVDT was cut, and the sample was removed.

For drying shrinkage testing, after 7 d of curing and demolding, the test was conducted on the concrete. The concrete column was placed vertically on the apparatus shown in Fig. 5b, with the bottom of the column fixed using a reserved hole. The top was leveled, and an LVDT was installed to record the linear changes in the concrete column during the drying process.

2.6. Seawater resistance test

The device used to simulate seawater immersion is shown in Fig. 6. The composition of the simulated seawater was based on previously published data[36–38]. The experimental procedure was as follows: (i) the concrete specimens were cured for 7 d after casting; (ii) the specimens were immersed in the simulated seawater for 12 h; (iii) the specimens were then air-dried with the aid of an electric fan. By repeating steps (ii) and (iii) for 150 cycles, the compressive strength was determined.

2.7. Rapid chloride migration test

The rapid chloride migration (RCM) test (Fig. 7)[39,40] was used to test the chloride migration coefficient when the concrete specimens had been cured for 4 weeks.

2.8. Characterization of pastes

The pastes of HESWBs were preferably selected from the composition in Section 2.2.1 with the ratio of water to binder of 0.4, while the compositions of the tested HESWBs were 38 wt% BFS, 38 wt% FA, 9.5 wt% DG, 9.5 wt% RM, and 5 wt% CS. Samples were cured at room temperature with (95±5)% RH until the required ages.

Electron Backscatter Diffraction (EBSD): The sample sections were embedded in epoxy resin (TRUER® MC001) and polished using SiC abrasive papers ranging from 800 to 3000 grit on a MaoPao 3® polishing machine (Veiyee). Further fine polishing was performed using 3 μm and 1 μm diamond suspensions. A thin conductive gold coating was then applied to the polished samples (30 mA for 30 s), followed by observation using an S-3400 N scanning electron microscope (Hitachi, Japan) under backscatter imaging mode with an accelerating voltage of 10 kV and a current of 60 mA.

2.9. Micro-XRF test

A micro-XRF equipment, M4 Tornado Micro-XRF (Bruker, Germany), was used to characterize the element distributions on the cross-sectional surface of both PC- and HESWB-based concretes[41,42]. The samples of concrete were cut from concrete samples in Section 2.2.2, and the testing surface was polished by a polishing machine with a diamond suspension as the polishing liquid.

3. Discussions

3.1. Fluidity and strength

The fluidity and compressive strength of HESWB-based mortars are shown in Fig. 8. Changing trends of fluidity and compressive strength are different. The fluidity affects the density of mortar, and the hydration process affects the final strength. This result shows a complex balance between the density and hydration process.

3.2. Hydration of HESWBs

To evaluate the differences in strength development and hydration behavior between Portland cement (PC) and high-entropy solid waste-based binders (HESWB), the compressive strength of mortar (w/b = 0.4) and hydration heat evolution are presented in Fig. 9a.

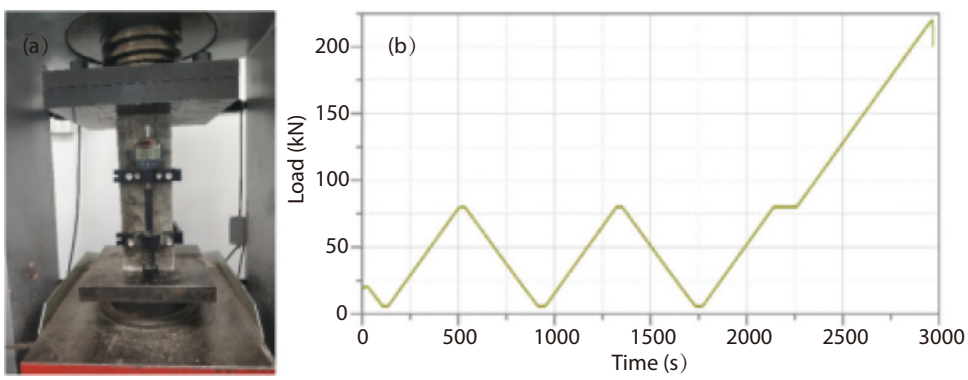


Fig. 4. Testing method of static elastic modulus.

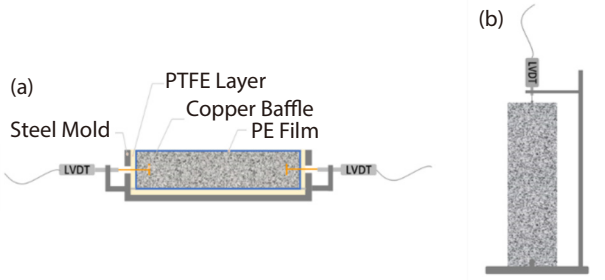


Fig. 5. Diagram of (a) autogenous and (b) drying shrinkage methods.

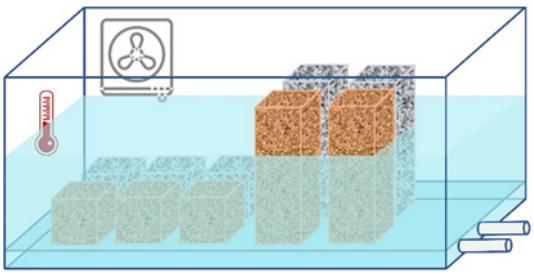


Fig. 6. Seawater corrosion simulation of concrete test set-up.

In terms of strength development, HESWB exhibits a similar trend to PC within the first 7 d. However, after this initial period, the strength gain of HESWB slows down compared to that of PC. Despite this slower rate, HESWB achieves a compressive strength of approximately 55 MPa at 28 d, which is still considered satisfactory for many structural applications.

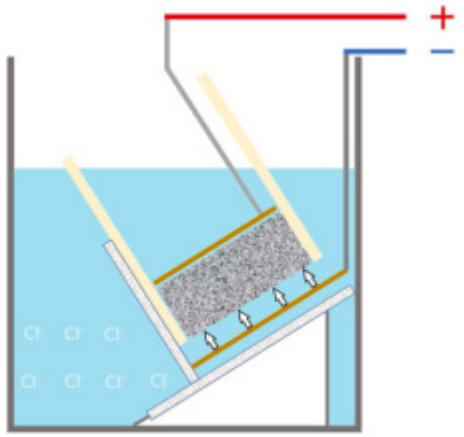


Fig. 7. Diagram of rapid chloride migration test set-up.

The hydration process of HESWB is quite different from that of PC, as shown in Fig. 9b. In its isothermal calorimetry, there are two main isothermal peaks in HESWB, similar to those in PC. The initial isothermal peak is obviously related to the moisture and dissolution of raw materials. The second one has a weak shoulder peak on the left of the main isothermal peak. Referring to others' reports[43–45] and the phases evolution analysis in the past, the shoulder peak is related to the formation of C-A-S-H gel, and the main isothermal peak corresponds to the AFt formation. In the PC paste, the second isothermal peak shows the initial hydration of C_3S[46–48]. The little shoulder peak is associated with the phase transition from AFt to AFm[49,50]. Moreover, the total cumulative heat

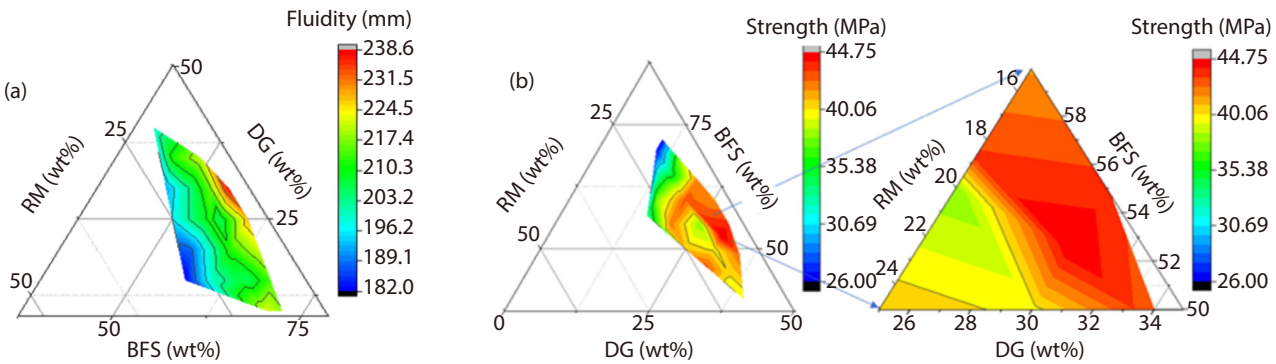


Fig. 8. (a) Fluidity and (b) compressive strength of HESWB-based mortars.

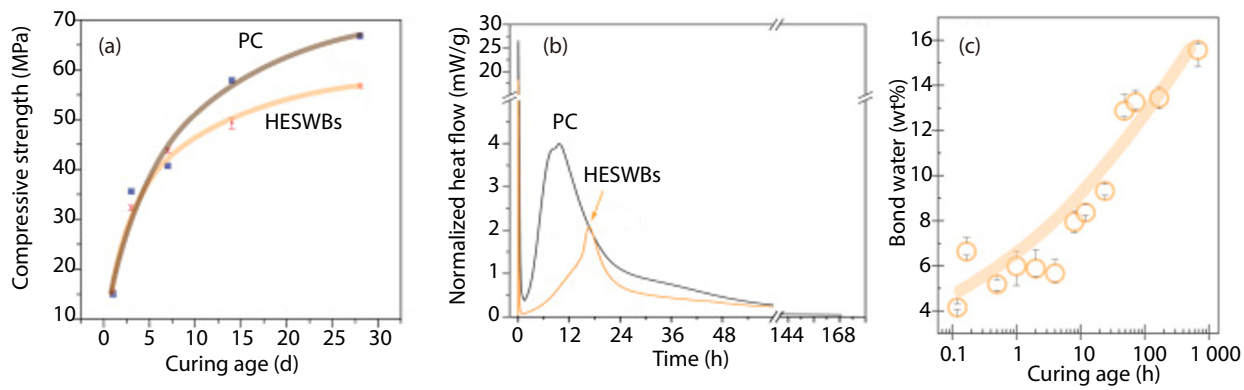


Fig. 9. Development of HESWB paste with *w/b* of 0.40 over different curing ages: (a) mechanical properties; (b) heat of hydration; (c) chemical bond water.

released over 7 d further highlights the difference in hydration kinetics. HESWB releases 177 J g^{-1} of heat, significantly lower than 327 J g^{-1} released by PC, indicating a lower overall degree of hydration within this period.

To further investigate the hydration process, the chemically bound water (CBW) content of HESWB paste was measured (Fig. 9c). The results indicate that AFt formation stabilizes within the first 7 d, after which the continued increase in CBW—from 5.66 wt% to 15.56 wt%—is primarily attributed to the ongoing formation of C-A-S-H gel.

Overall, while HESWB shows comparable early strength development to PC, its hydration process is distinctly different, characterized by lower heat release, delayed pozzolanic reactions, and greater reliance on the formation of C-A-S-H gel rather than C_3S hydration.

3.3. Microstructures in HESWBs

In Fig. 10, the EBSD images show the representative microstructure of HESWBs. The main matrices are unhydrated raw materials, including BFS particles, spherical FA particles, and fine RM particles with high Na content. The hydrates are filled between these unhydrated raw materials and are connected to these particles. The unclear rim of BFS suggests that BFS is the main hydration reactant. In contrast, the clear rims of FA and RM indicate that they mainly act as fillers during the early curing stages of the HESWB paste.

Fig. 11 shows the main chemical components of the rim around BFS. Based on the element testing by the EBSD, the Ca/Si, Al/Si, and Al/Ca molar ratios are 1.39, 0.62, and 0.45, respectively, in BFS, and these molar ratios in the unclear rim are 1.19, 0.79, and 0.66, respectively. The chemical components of this low-Ca rim are similar to those of the reported C-A-S-H gel in alkali-activated slag[51]. The chemical components difference between BFS and the rim area shows a decalcification during the BFS reaction (Fig. 11)[52,53]. The dis-

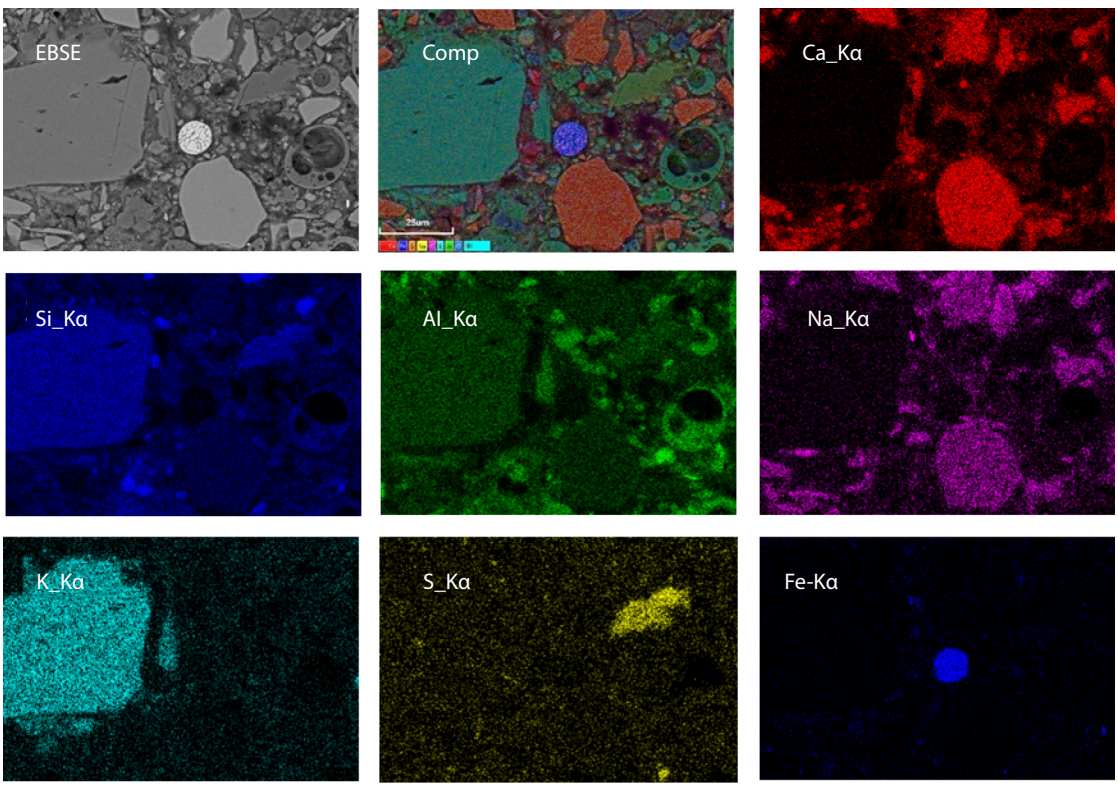


Fig. 10. SEM image of HESWB paste.

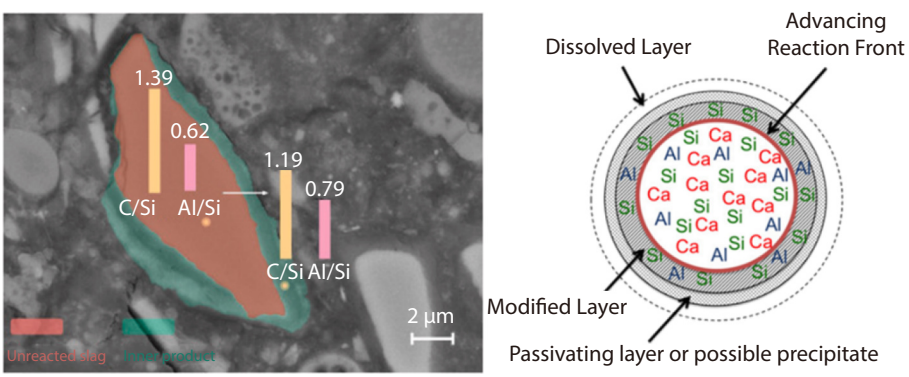


Fig. 11. C-A-S-H gel rim around slag particles and its semi-quantitative compositions by EBSD.

solved Ca plays a vital role in the formation of AFt. According to the study by Irbe et al.[54], in the C-A-S-H gel synthesis process, AFt would appear if the solution is CH-saturated. High-Ca-type C-A-S-H gel often shows higher mechanical performance, and the decalcification phenomenon would reduce the calcium proportion in C-A-S-H gel. Therefore, an extra calcium supplement would be necessary in the HESWB system. Lime[55,56], CH[57], cement clinkers[58], and carbide slag[59,60] in appropriate dosages added to the HESWB system could supply calcium in C-A-S-H gel and AFt formation, thus strongly enhancing the mechanical properties of HESWB. These complex interactions between raw materials of HESWBs show an obvious cocktail effect of high-entropy materials. When a new component is introduced in the current binder system, its chemical composition, alkalinity, particle shape and size, and other properties would affect the hydration process and the final mechanical properties and durability. In the following sections, the roles of different raw materials in the HESWB system will be discussed in detail.

3.4. Role of FA

The fluidity and strength of HESWBs with different FA contents are shown in Fig. 12. In the HESWBs, FA does not have the lubrication effect[61,62], which might be due to its higher water requirement. Both compressive and flexural strengths decrease with the increase in FA content in HESWBs.

Fig. 13 shows the heat release of HESWBs with different FA content. Although the FA content increases significantly, the initial heat release only slightly decreases. The initial reaction is not inhibited by FA. This phenomenon indicates the stability of the initial reaction process.

In Fig. 14, the FA in HESWBs does not react significantly. Its morphology still keeps a spherical structure.

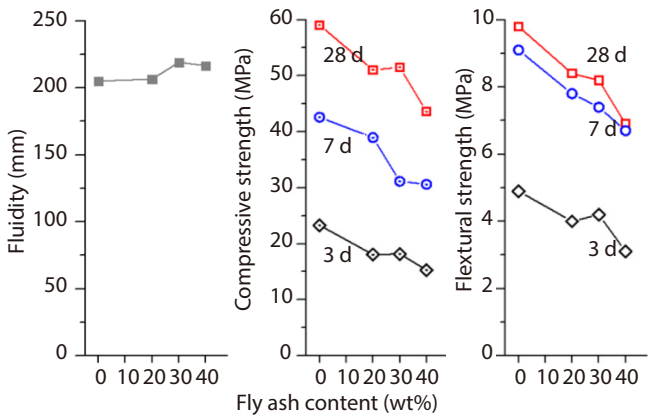


Fig. 12. Fluidity and strength of HESWB-based mortars with different FA content.

3.5. Role of RM

Compressive strength of HESWB-based mortars with different RM contents at 28 d is shown in Fig. 15. RM is a highly alkaline solid waste, and the alkaline metal in it would significantly decrease the strength of Portland concrete. However, when the RM content increases, the compressive strength of HESWB-based mortars increases. The alkalinity of RM is helpful to the strength[63]. This effect is contrary to that in the Portland system[64,65]. Compared to the result in Fig. 12, FA has quite a low hydration activity, and the strength decreases with the increase of FA dosages. In contrast, the strength increases by about 4.9 MPa, which is a significant change.

Fig. 16 shows the effect of RM on the heat release of HESWB pastes. The alkalinity strongly accelerates the hydration reaction[66], and the main peak is advanced to about 4 h. Meanwhile, the initial cumulative heat release increases. It indicates that more products are generated, and it might be related to the alkali-activated reaction of alkaline substance and slag.

Fig. 17 shows the SEM images of HESWB pastes containing RM at 28 d. AFt is generated at the surface of slag or other particles of raw materials. The size of AFt (needle-like phase in yellow frames) is small after adding RM in HESWBs, which suggests the modification effect of alkaline metal ions on the products[67,68].

The pore size distributions are shown in Fig. 18, and total porosities are shown in Table 4. The average pore size dramatically reduces after adding RM. The most probable pore size reduces from 0.1–0.2 μm to 0.01–0.02 μm. The total porosity decreases by more than half. This also shows the positive effect of RM on the density of HESWBs. To further analyze the change of the volume fractions of pore size distributions, the pore structure is divided into gel nano-pores (<10 nm), small to medium pores (10–50 nm), medium capillary pores (50–100 nm), large capillary pores (100–5000 nm), and macropores (>5000 nm)[69], as shown in Fig. 19. For both samples in Fig. 19, there is a similar trend. Although the macropores belong to cracks and entrained air during the preparation pro-

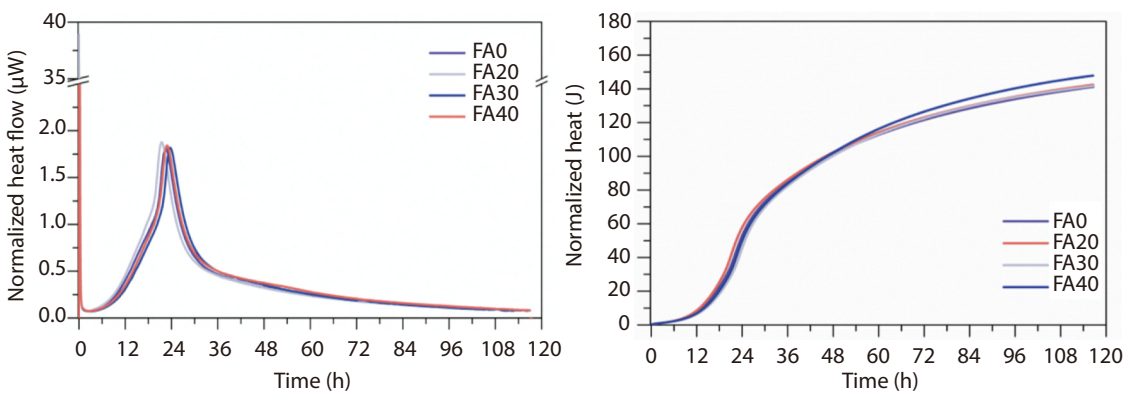


Fig. 13. Heat release of HESWB pastes with different FA content.

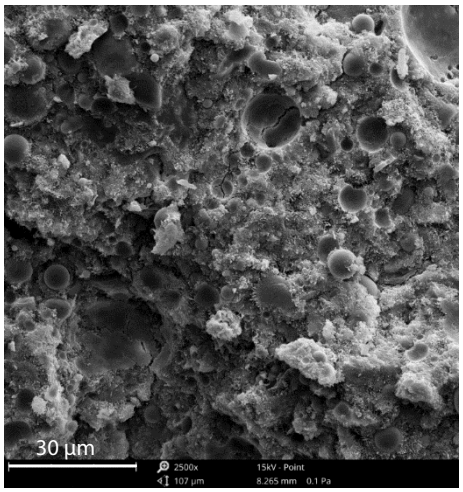


Fig. 14. SEM image of HESWB paste containing FA at 28 d.

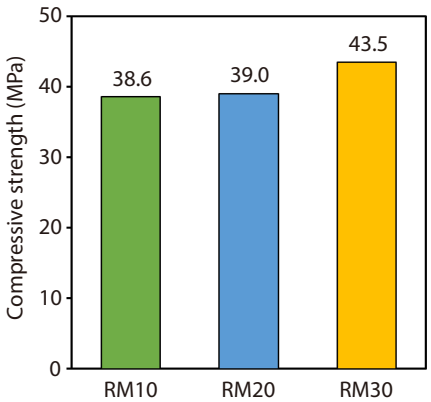


Fig. 15. Compressive strength of HESWB-based mortars with different RM contents at 28 d.

cess, this part of the pore structure is excluded. The introduction of RM significantly reduces the proportion of large capillary pores of the main matrix. As the dosage of RM increases from 10 wt% to 20 wt%, the proportion of small to medium pores reduces, but the strength increases by 0.4 MPa. When the dosage of RM is 30 wt%, the volume fractions are similar, but the strength increases by about 4.9 MPa. The increase in strength should be related to the enhanced hydration process of RM.

It can be concluded that RM shows a dual action in the HESWB-based material. The filling effect refines the pore structure, and the alkalinity enhances the hydration process.

3.6. Role of CS

Fig. 20 shows the heat release of HESWB paste with different CS contents. The main peak is advanced due to the alkaline substance in CS. CS contains portlandite, and it can accelerate the main hydration reaction[70]. The cumulative heat release is close, and increasing the CS contents does not promote the cumulative heat release. The pore size distributions of HESWB pastes with different CS contents are shown in Fig. 21, and the volume fractions are shown in Fig. 22. Different from RM, CS increases the most probable pore size at both 7 d and 28 d. For the volume fractions, large capillary pores increase to about 50%, which significantly inhibits the strength development.

In the SEM images in Fig. 23, the morphology of products in HESWBs changes with the increase in CS. At 3 d, the needle-like product decreases due to the CS, but some of this product is formed at 60 d.

Both CS and RM can accelerate the hydration reaction, but the accelerating patterns are different[71,72]. The effect of alkaline substance type on the hydration process is complex. This shows the unpredictability of alkaline substances on the HESWBs, which indicates a significant cocktail effect.

3.7. Performance of HESWB-based concrete

The mechanical properties of PC-based and HESWB-based concretes are shown in Fig. 24. Because the mixed design is based on the same volume paste rule, the mass of the PC is higher than that of HESWB. The *w/b* ratio in PC-based concrete is 0.35, which is lower than that (0.38) in HESWB-based concrete. Hence, the compressive strength of PC-based concrete is higher than that of HESWB-based concrete at all ages. The compressive strength growth rate of PC-based concrete is also faster than that of HESWB-based concrete. Moreover, the effect of aggregate types on the compressive strength is weak. In both binder type-based concretes, the differences in compressive strength are lower than 7 MPa at all ages.

The stress-strain curves of both concretes are shown in Fig. 25. The stress-strain curve of HESWB-based concrete is lower than that of PC-based concrete. The static modulus of elasticity of HESWB-based concrete is lower, regardless of the aggregate types. For example, for specimens aged for 28 d,

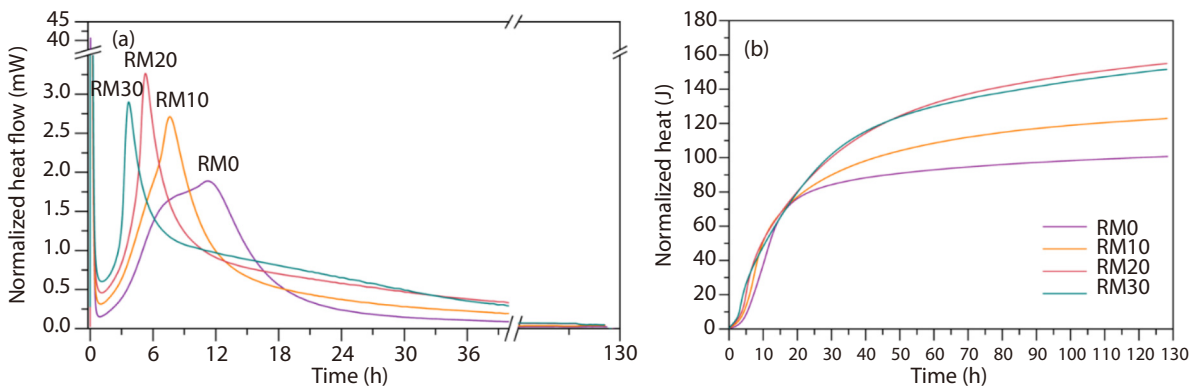


Fig. 16. Heat release of HESWB pastes with different RM contents.

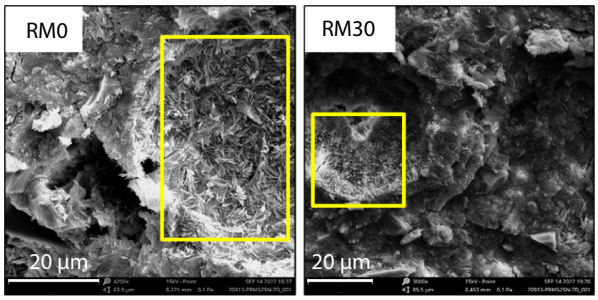


Fig. 17. SEM images of HESWB pastes containing RM at 28 d.

PC_N exhibited the highest modulus of 37.73 GPa, while PC_A modulus was 27.11 GPa, and HESWB_N modulus was 28.67 GPa, although their uniaxial compressive strength levels were the same (36.8–40.3 MPa).

Fig. 26 shows the autogenous and drying shrinkage of PC- and HESWB-based concrete. First, the different binder systems used in this study resulted in various shrinkage developments of the concretes. For PC-based concrete, the specimens exhibited continuous shrinkage at the studied ages, including autogenous shrinkage (up to about 7 d) and drying shrinkage (up to 28 d). For HESWB-based concretes, an expansion in autogenous shrinkage was observed at initial days, and this period corresponded to the time of ettringite formation. Thus, the HESWB-based concrete showed slight expansion at the early ages. With the further hydration of HESWBs, the matrix became compacted, and autogenous shrinkage was observed. For both PC-based and HESWB-based systems,

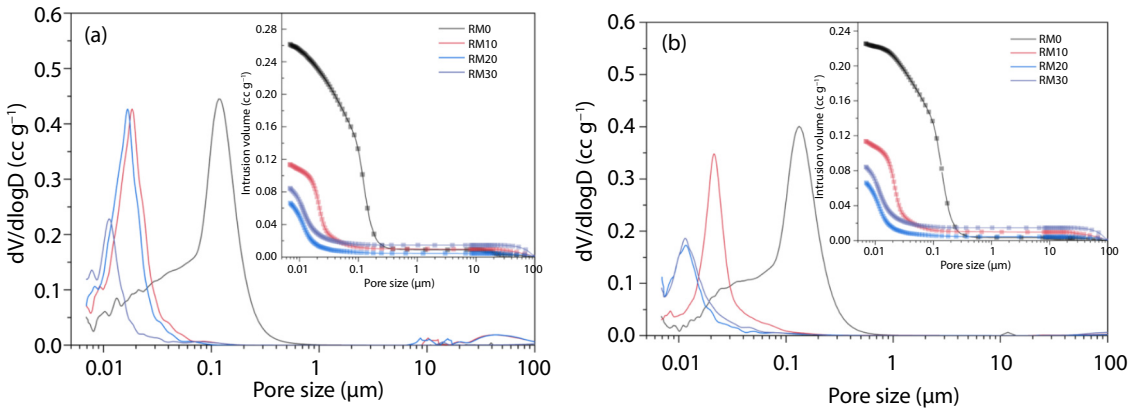


Fig. 18. Pore size distributions of HESWB pastes with different RM contents at (a) 7 d and (b) 28 d.

Table 4. Total porosity data for HESEM samples with varying RM content (cc g^{-1}).

Samples	7 d	28 d
RM0	0.253	0.222
RM10	0.105	0.104
RM20	0.063	0.062
RM30	0.071	0.070

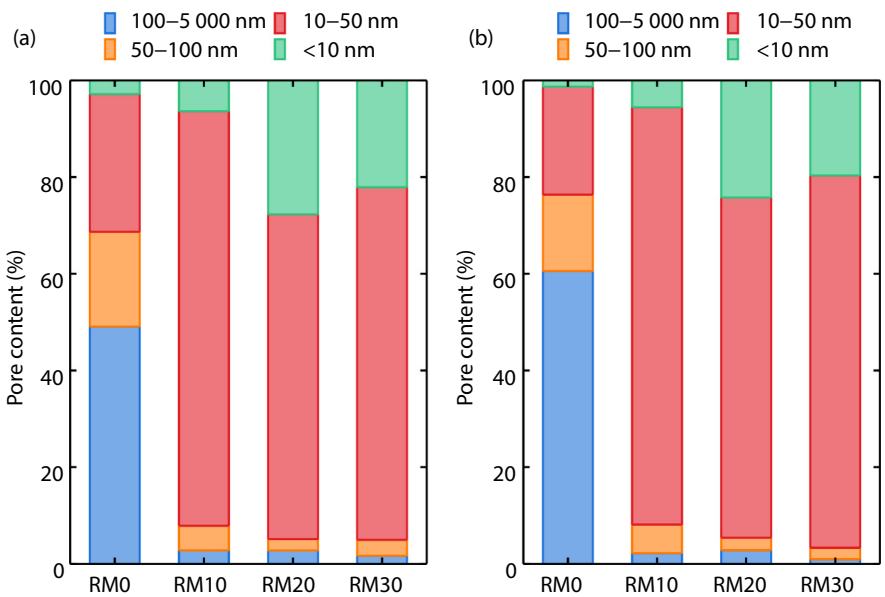


Fig. 19. Volume fractions of pore size distributions of HESWB pastes containing RM at different curing ages: (a) 7 d; (b) 28 d.

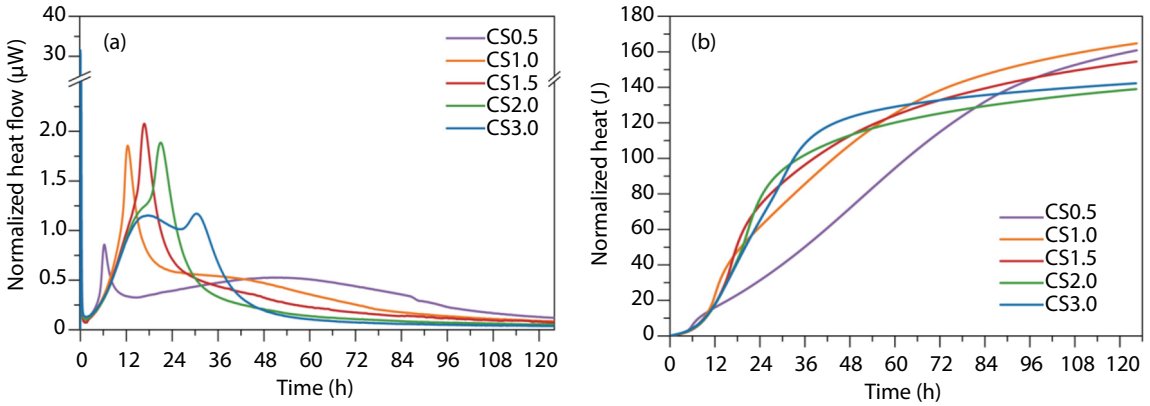


Fig. 20. Heat release of HESWB pastes with different CS contents.

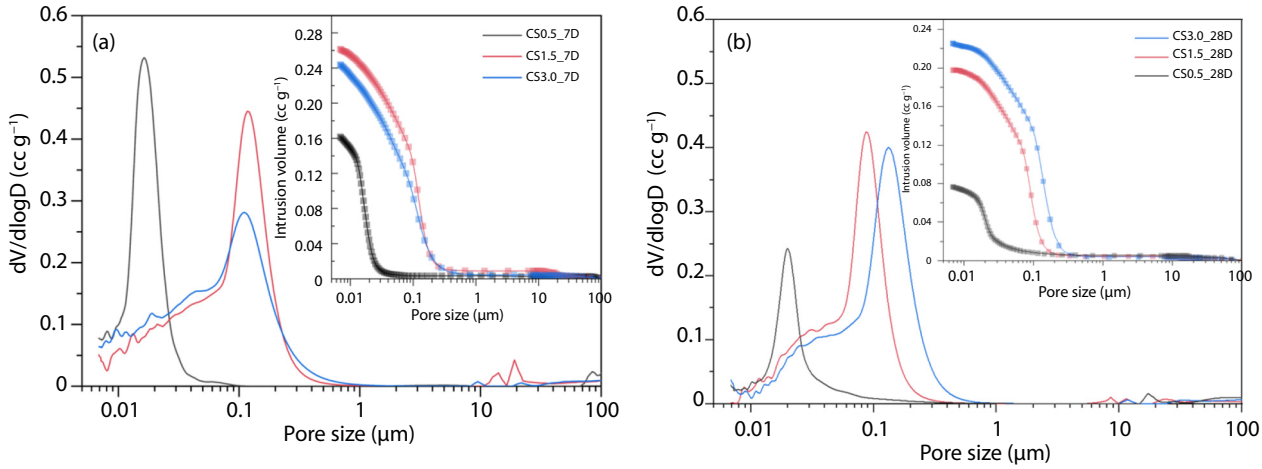


Fig. 21. Pore size distributions of HESWB pastes with different CS contents at (a) 7 d and (b) 28 d.

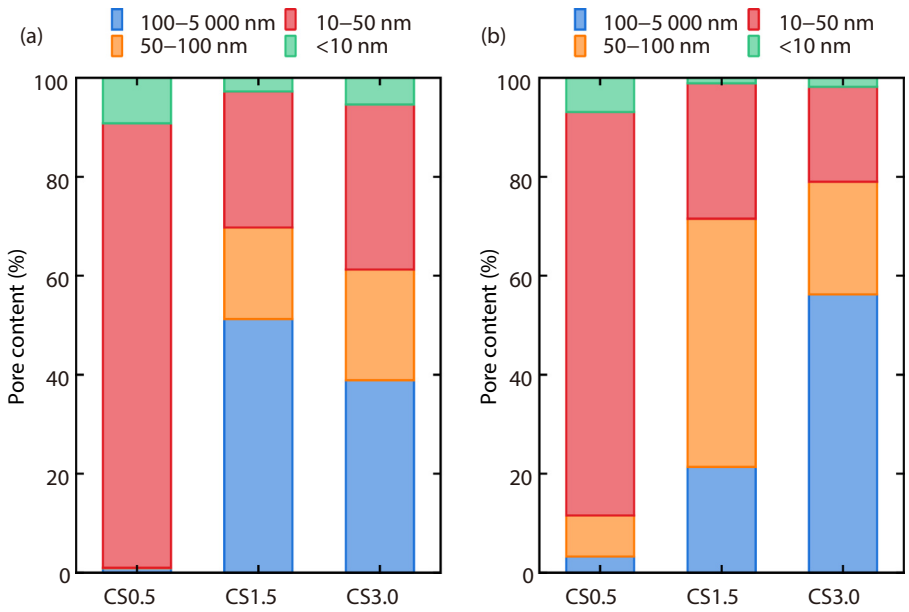


Fig. 22. Volume fractions of pore size distributions of HESWB pastes within CS at different curing ages: (a) 7 d; (b) 28 d.

the use of artificial aggregates led to a significant reduction in autogenous shrinkage compared with concretes containing the same binders. Artificial aggregates reduced the self-desiccation of the concrete[73]. Another significant result in autogenous shrinkage implied that HESWBs' hydration caused more significant autogenous shrinkage, which could be attributed to the much higher slag content in HESWBs. It is well known that a much higher incorporation of slag in binders would cause more severe shrinkage of concrete[74–77]. PC-based concrete exhibited almost double the drying shrinkage compared to its HESWB-based counterparts. As reported by others, HESWB-based concrete showed much lower dry-

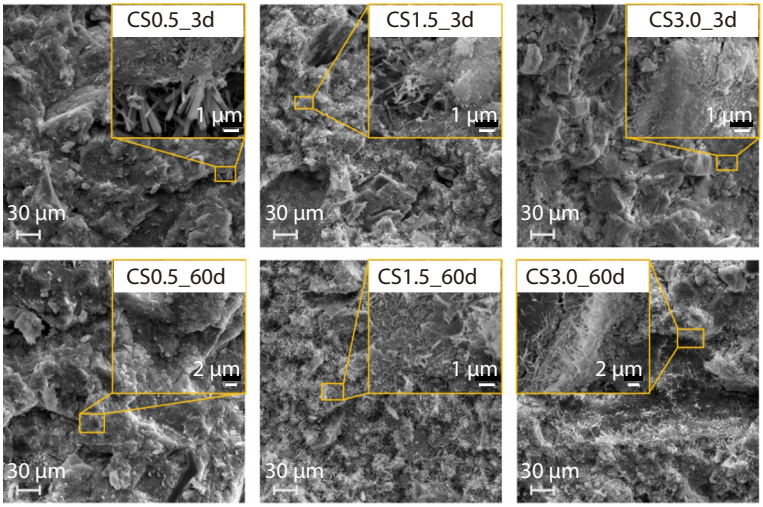


Fig. 23. SEM images of HESWB pastes containing CS at 3 d and 60 d.

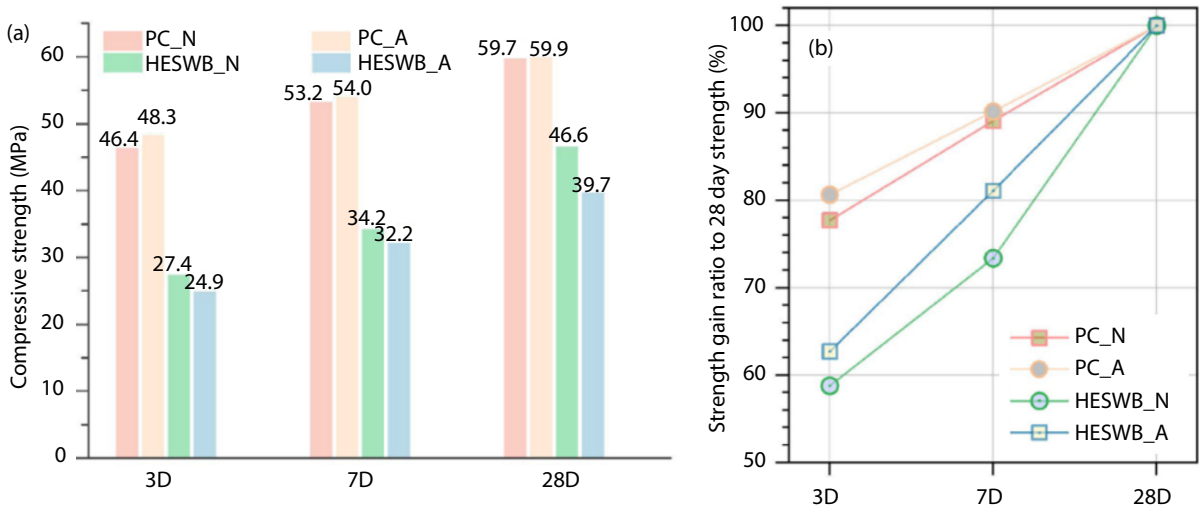


Fig. 24. (a) Compressive strength development and (b) compressive strength growth rate relative to 28 d compressive strength of PC-based concrete and HESWB-based concrete.

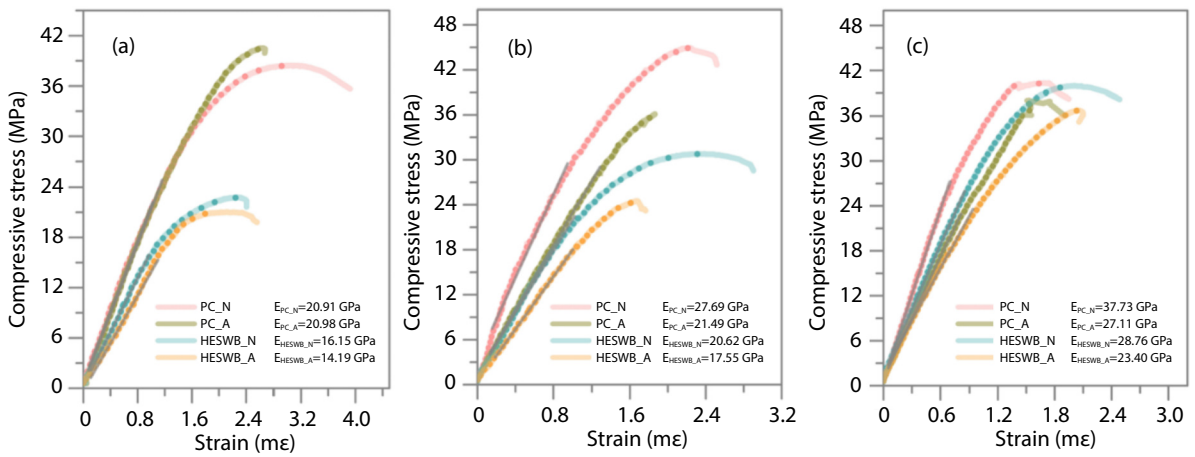


Fig. 25. Stress–strain curves and static modulus of elasticity of normal PC-based concretes and HESWB-based concretes at (a) 3 d, (b) 7 d, and (c) 28 d.

ing shrinkage than PC-based concrete[43,78,79]. Replacing natural aggregates with artificial ones caused a slight increase in drying shrinkage in both PC- and HESWB-based concretes.

Autogenous shrinkage and drying shrinkage are governed by distinct mechanisms, thus exhibiting different trends without contradiction. Autogenous shrinkage primarily results from internal water consumption during the hydration process, particularly under sealed conditions,

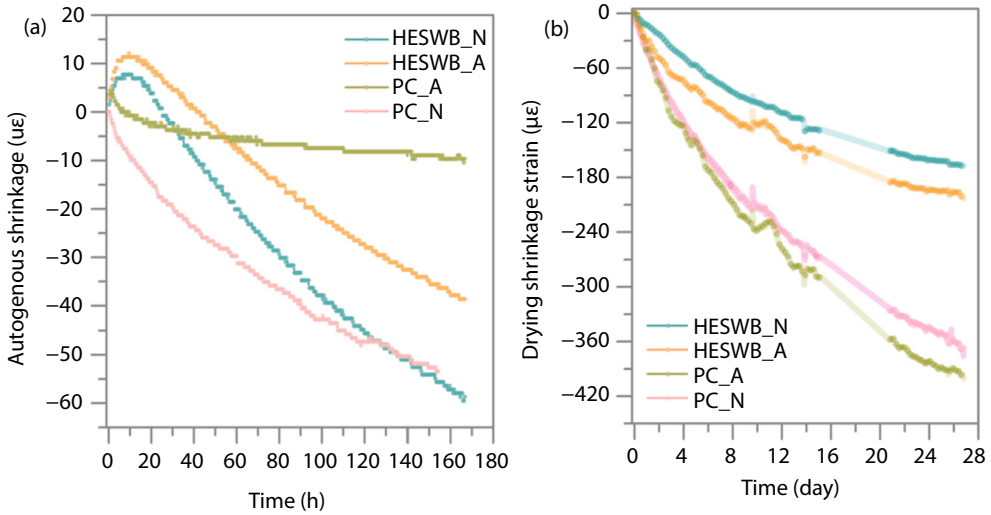


Fig. 26. (a) Autogenous shrinkage and (b) drying shrinkage of PC-based concrete and HESWB-based concrete.

where self-desiccation occurs as hydration products form. In contrast, drying shrinkage is driven by the evaporation of pore water to the external environment, leading to capillary tension and volume reduction. The micro-expansive behavior observed in HESWB is largely attributed to the early formation of ettringite (AFt), which can locally counteract shrinkage strains, especially during the early drying stage. Although HESWB concrete exhibits greater autogenous shrinkage than PC concrete because of its faster hydration and higher internal water consumption, it tends to show lower drying shrinkage. This suggests that HESWB retains less water during the drying process, indicating a lower water-holding capacity compared to PC. Therefore, the observed differences in autogenous and drying shrinkage are not contradictory but reflect the distinct influences of hydration kinetics and moisture transport characteristics on the two systems.

Fig. 27 shows the RCM test results of the four kinds of prepared concretes. Fig. 27a displays the Cl^- penetration depth indicated by $AgNO_3$. In PC-based concrete, apparent lighter profiles can be identified at the front of Cl^- penetration, while for HESWB-based concrete, no determinable Cl^- migration profile can be found. For PC_N concrete, the Cl^- penetration depth is 15.10 mm, and that of PC_A concrete is 9.78 mm. Interestingly, it is found that the incorporation of artificial aggregates can improve the chloride attack performance of PC-based concrete. For HESWB-based concrete, no AgCl profiles were observed, so the indicator may be unsuitable for HESWB-based concrete, or the HESWB paste may have suppressed Cl^- penetration. Therefore, a test device similar to the rapid chloride permeability test but with smaller specimen dimensions (Φ50 mm × H50 mm) has been used to evaluate the paste conductivity. At the same external voltage, the current through the PC paste is above 20 mA throughout the test period, while the current through the HESWB paste is only 3–4 mA. Thus, in the RCM test, the external electric field doesn't accelerate the Cl^- mitigation. The extremely low conductivity results in significantly lower chloride diffusion parameters. Therefore, HESWB-based concrete presents extremely excellent chloride resistance compared with PC-based concrete[80,81].

A promising application scenario for AFt-bearing binder hydrates is in marine engineering materials. Therefore, the resistance of concrete to seawater has been the main focus in this part. As shown in Fig. 28a, the appearances of the four

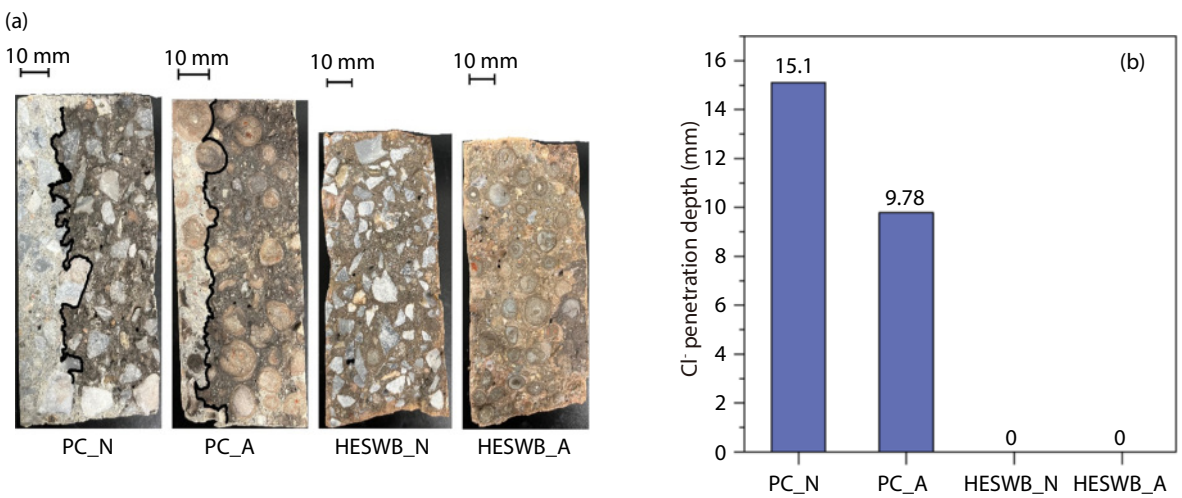


Fig. 27. (a) Cl^- penetration depth of concrete; (b) Cl^- migration coefficients determined by the RCM method.

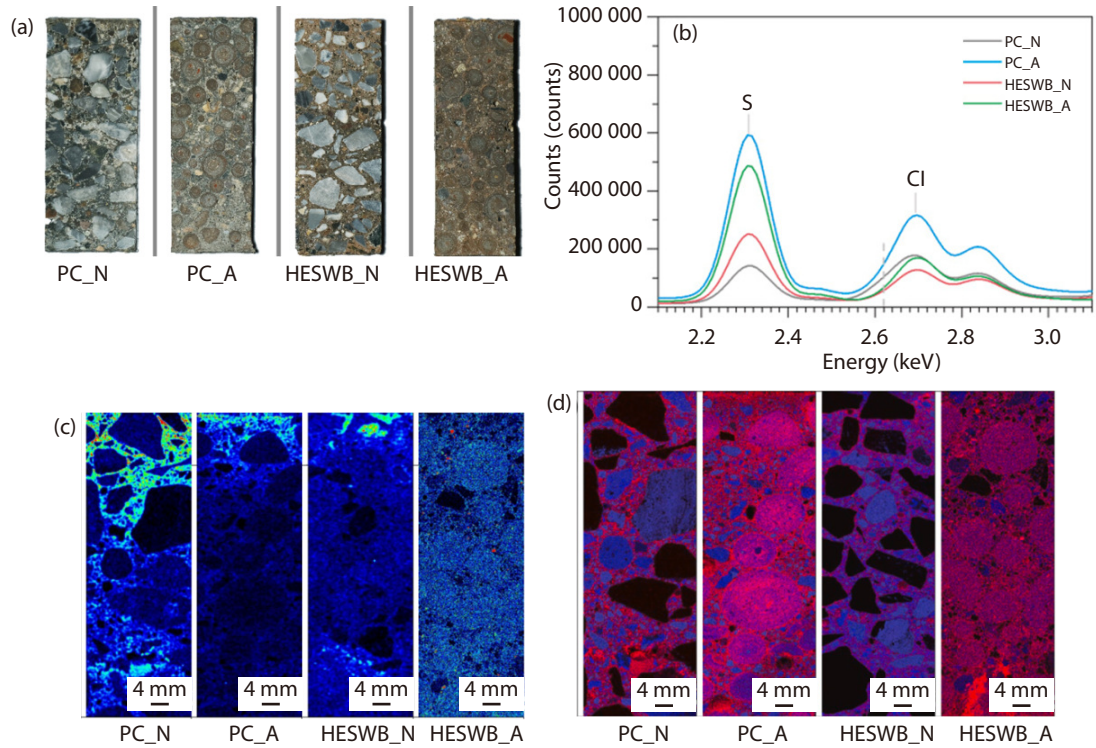


Fig. 28. (a) Appearance of cross section of four kinds of concrete; (b) S and Cl element spectrum; (c) Cl and (d) S element penetration profiles in the seawater invasion experiments.

kinds of concrete have yet to present significant degradation after 150 times of seawater erosion. Figs. 28c and d present the micro-XRF results of concrete after seawater corrosion. A much higher S intensity is observed for HESWB-based concrete (see Fig. 28b) due to the higher S content. Fig. 28c presents the Cl^- penetration profiles of concrete. It was found that PC_N exhibited the greatest increase in penetration depth, and the penetration depths of PC-based concrete were larger than those of HESWB-based concrete overall. It clearly showed that HESWB-based concrete performed better against Cl^- attacks. Based on the results from Cl^- migration experiments, Cl^- migration coefficients of HESWB-based concretes were nearly unavailable in the RCM test, further evidencing their excellent Cl^- resistance. Meanwhile, S ion penetration profiles of the four kinds of concrete have also been estimated[82], as shown in Fig. 28d. Due to the higher S content used in HESWBs, the S signal intensity is much higher in HESWB-based concrete and artificial aggregates. However, no apparent sulfur gradient was observed in the micro-XRF test, and no degradation was observed[83].

4. Conclusions

Referring to the principle of HEMs, a novel concept of HESWB is proposed. A multi-component binder prepared by BFS, FA, RM, DG, and CS is investigated, and the performance of HESWB-based concrete is analyzed. Some conclusions are as follows:

(1) The HESWBs exhibit high-entropy characteristics. This is evident from their diverse composition, the disordered structural features of the raw materials, the variety of hydration products, and a higher degree of polymerization. These properties highlight the complex and highly entropic nature of these materials, which contributes to their unique performance characteristics.

(2) HESWBs can achieve performance levels comparable to Portland cement (P.O. 42.5). This is accomplished through the complementary composition of raw materials and the synergistic effects during hydration. The interaction between different waste components enhances the material's properties, making it a viable alternative to traditional cement in various applications.

(3) HESWBs offer exceptional durability advantages, including micro-expansion and high resistance to chloride ion penetration and sulfate attack. These features make them particularly suitable for use in environments exposed to harsh conditions. The material's durability suggests significant potential for applications in road engineering, cement and concrete products, and artificial aggregates, indicating a broad scope for future use.

Author contribution statement

Dongmin Wang: Conceptualization & Funding acquisition. **Huangqi Wang:** Writing – original draft. **Peiliang Shen:** Formal analysis. **Jixiang Wang:** Data curation & Investigation. **Rui Sun:** Writing – review & editing. **Bo Liu:** Formal analysis. **Moncef Nehdi:** Formal analysis & Methodology. All the authors have approved the final manuscript.

Declaration of competing interest

Dongmin Wang is the Editor-in-Chief, and Peiliang Shen is the Associate Editor for *Materials Reports: Solidwaste and Ecomaterials*. They were not involved in the editorial review or

the decision to publish this article. The authors declare that they have no known competing financial interests or personal relationships that could have appeared to influence the work reported in this paper.

Acknowledgements

The authors would like to acknowledge the Chinese National Natural Science Foundation Regional Innovation and Development Joint Fund (No. U20A20313), the National Key Research and Development Program of China (No. 2024YFB3714800), and Henan Provincial Huanghuai Laboratory Innovation Special Project (No. 240700003).

References

[1] Oses, C., Toher, C., Curtarolo, S. High-entropy ceramics. *Nature Reviews Materials*, **2020**, 5(4): 295–309. https://doi.org/10.1038/s41578-019-0170-8.

[2] Qian, X., Han, D., Zheng, L., et al. High-entropy polymer produces a giant electrocaloric effect at low fields. *Nature*, **2021**, 600(7890): 664–669. https://doi.org/10.1038/s41586-021-04189-5.

[3] Dou, L., Yang, B., Lan, S., et al. High-entropy-nanofibers enhanced polymer nanocomposites for high-performance energy storage. *Advanced Energy Materials*, **2023**, 13(11): 2203925. https://doi.org/10.1002/aenm.202203925.

[4] Hsu, W. L., Tsai, C. W., Yeh, A. C., et al. Clarifying the four core effects of high-entropy materials. *Nature Reviews Chemistry*, **2024**, 8(6): 471–485. https://doi.org/10.1038/s41570-024-00602-5.

[5] Tsai, M. H., Yeh, J. W. High-entropy alloys: A critical review. *Materials Research Letters*, **2014**, 2(3): 107–123. https://doi.org/10.1080/21663831.2014.912690.

[6] Ding, Q., Zhang, Y., Chen, X., et al. Tuning element distribution, structure and properties by composition in high-entropy alloys. *Nature*, **2019**, 574(7777): 223–227. https://doi.org/10.1038/s41586-019-1617-1.

[7] Yeh, J. W., Chen, S. K., Lin, S. J., et al. Nanostructured high-entropy alloys with multiple principal elements: Novel alloy design concepts and outcomes. *Advanced Engineering Materials*, **2004**, 6(5): 299–303. https://doi.org/10.1002/adem.200300567.

[8] Rao, Z., Tung, P. Y., Xie, R., et al. Machine learning–enabled high-entropy alloy discovery. *Science*, **2022**, 378(6615): 78–85. https://doi.org/10.1126/science.abo4940.

[9] Scrivener, K. L., Juilland, P., Monteiro, P. J. M. Advances in understanding hydration of Portland cement. *Cement and Concrete Research*, **2015**, 78: 38–56. https://doi.org/10.1016/j.cemconres.2015.05.025.

[10] Fang, K., Zhao, J., Wang, D., et al. Use of ladle furnace slag as supplementary cementitious material before and after modification by rapid air cooling: A comparative study of influence on the properties of blended cement paste. *Construction and Building Materials*, **2022**, 314: 125434. https://doi.org/10.1016/j.conbuildmat.2021.125434.

[11] Yuan, N., Wang, S., Chen, T., et al. Comparative effects of the pristine and amino-functionalized metal–organic frameworks on the mechanical properties and microstructures of cement pastes. *Construction and Building Materials*, **2022**, 347: 128544. https://doi.org/10.1016/j.conbuildmat.2022.128544.

[12] Wang, H., Dong, Z., Wang, D. Preliminarily evaluation of poly (AA-co-AMPS) on the properties of sulphoaluminate cement. *Construction and Building Materials*, **2022**, 347: 128571. https://doi.org/10.1016/j.conbuildmat.2022.128571.

[13] Wang, H., Zhang, L., Wang, D., et al. Stability of phenyl copolymer–graphene oxide composites in high-alkali and/or-calcium environments: Implications for strengthening and toughening cement-based materials. *ACS Applied Nano Materials*, **2022**, 5(3): 4038–4047. https://doi.org/10.1021/acsanm.2c00023.

[14] Wang, H., Zhang, L., Wang, D., et al. Dispersion of graphene oxide and its application prospect in cement-based materials: A review. *Journal of Dispersion Science and Technology*, **2023**, 44(3): 392–405. https://doi.org/10.1080/01932691.2021.1948423.

[15] Shen, P., Lu, L., He, Y., et al. The effect of curing regimes on the mechanical properties, nano-mechanical properties and microstructure of ultra-high performance concrete. *Cement and Concrete Research*, **2019**, 118: 1–13. https://doi.org/10.1016/j.cemconres.2019.01.004.

[16] Shen, P., Lu, L., He, Y., et al. Investigation on expansion effect of the expansive agents in ultra-high performance concrete. *Cement and Concrete Composites*, **2020**, 105: 103425. https://doi.org/10.1016/j.cemconcomp.2019.103425.

[17] Wang, S., Gu, X., Liu, J., et al. Assessment of lithium slag as a supplementary siliceous material in autoclaved aerated concrete: Physical properties and hydration characteristics. *Construction and Building Materials*, **2024**, 442: 137621. https://doi.org/10.1016/j.conbuildmat.2024.137621.

[18] Yang, H., Cui, H., Tang, W., et al. A critical review on research progress of graphene/cement based composites. *Composites Part A: Applied Science and Manufacturing*, **2017**, 102: 273–296. https://doi.org/10.1016/j.compositesa.2017.07.019.

[19] Cui, H., Zhang, L., Yang, H., et al. Optimizing thermal comfort and energy efficiency in hospitals with PCM-Enhanced wall systems. *Energy and Buildings*, **2024**, 323: 114740. https://doi.org/10.1016/j.enbuild.2024.114740.

[20] Li, Q., Ma, H., Tang, Y., et al. Combined effect of $NaAlO_2$ and NaOH on the early age hydration of Portland cement with a high concentration of borate solution. *Cement and Concrete Research*, **2021**, 144: 106430. https://doi.org/10.1016/j.cemconres.2021.106430.

[21] Li, X., Sun, R., Wang, D., et al. Insights into the acid-modification on magnesium slag and its effects on cement-magnesium slag composite cementitious material. *Construction and Building Materials*, **2024**, 449: 138445. https://doi.org/10.1016/j.conbuildmat.2024.138445.

[22] Wang, J., Ren, C., Huang, T., et al. Performances of concrete with binder and/or aggregates replacement by all-solid waste materials. *Journal of Cleaner Production*, **2024**, 450: 141929. https://doi.org/10.1016/j.jclepro.2024.141929.

[23] Sun, R., Shen, P., Wang, D., et al. Enhancing hydration of steel slag-based composite cementitious material: Synergistic effect of triisopropanolamine (TIPA) and sulfite/sulfate. *Cement and Concrete Research*, **2024**, 184: 107619. https://doi.org/10.1016/j.cemconres.2024.107619.

[24] Wang, J., Huang, T., Ren, C., et al. Internal carbonation reinforcement of cementitious materials: Mechanism and performance. *Journal of Building Engineering*, **2023**, 77: 107491. https://doi.org/10.1016/j.jobe.2023.107491.

[25] Lu, J. X., Shen, P., Ali, H. A., et al. Mix design and performance of lightweight ultra high-performance concrete. *Materials & Design*, **2022**, 216: 110553. https://doi.org/10.1016/j.matdes.2022.110553.

[26] Shen, P., Zheng, H., Xuan, D., et al. Feasible use of municipal solid waste incineration bottom ash in ultra-high performance concrete. *Cement and Concrete Composites*, **2020**, 114: 103814. https://doi.org/10.1016/j.cemconcomp.2020.103814.

[27] Zhang, Z., Provis, J. L., Reid, A., et al. Geopolymer foam concrete: An emerging material for sustainable construction. *Construction and Building Materials*, **2014**, 56: 113–127. https://doi.org/10.

1016/j.conbuildmat.2014.01.081.
[28] Cakiroglu, C., Batool, F., Islam, K., et al. Explainable ensemble learning predictive model for thermal conductivity of cement-based foam. *Construction and Building Materials*, **2024**, 421: 135663. https://doi.org/10.1016/j.conbuildmat.2024.135663.
[29] Jamali, A., Marani, A., Railton, J., et al. Novel multi-scale experimental approach and deep learning model to optimize capillary pressure evolution in early age concrete. *Cement and Concrete Research*, **2024**, 180: 107490. https://doi.org/10.1016/j.cemconres.2024.107490.
[30] Yaseen, Z. M., Deo, R. C., Hilal, A., et al. Predicting compressive strength of lightweight foamed concrete using extreme learning machine model. *Advances in Engineering Software*, **2018**, 115: 112–125. https://doi.org/10.1016/j.advengsoft.2017.09.004.
[31] Ben Chaabene, W., Flah, M., Nehdi, M. L. Machine learning prediction of mechanical properties of concrete: Critical review. *Construction and Building Materials*, **2020**, 260: 119889. https://doi.org/10.1016/j.conbuildmat.2020.119889.
[32] Juenger, M. C. G., Winnefeld, F., Provis, J. L., et al. Advances in alternative cementitious binders. *Cement and Concrete Research*, **2011**, 41(12): 1232–1243. https://doi.org/10.1016/j.cemconres.2010.11.012.
[33] Shi, C., Qu, B., Provis, J. L. Recent progress in low-carbon binders. *Cement and Concrete Research*, **2019**, 122: 227–250. https://doi.org/10.1016/j.cemconres.2019.05.009.
[34] Mao, Y., Liu, J., Shi, C. Autogenous shrinkage and drying shrinkage of recycled aggregate concrete: A review. *Journal of Cleaner Production*, **2021**, 295: 126435. https://doi.org/10.1016/j.jclepro.2021.126435.
[35] Huang, L., Chen, Z., Ye, H. A mechanistic model for the time-dependent autogenous shrinkage of high performance concrete. *Construction and Building Materials*, **2020**, 255: 119335. https://doi.org/10.1016/j.conbuildmat.2020.119335.
[36] Cai, Y., Xuan, D., Hou, P., et al. Effect of seawater as mixing water on the hydration behaviour of tricalcium aluminate. *Cement and Concrete Research*, **2021**, 149: 106565. https://doi.org/10.1016/j.cemconres.2021.106565.
[37] Narvaez-Montoya, C., Mahlknecht, J., Torres-Martínez, J. A., et al. Seawater intrusion pattern recognition supported by unsupervised learning: A systematic review and application. *Science of the Total Environment*, **2023**, 864: 160933. https://doi.org/10.1016/j.scitotenv.2022.160933.
[38] Zhang, Z., Dai, J., Liu, J., et al. Enhancing energy–climate–economy sustainability in coastal cities through integration of seawater and solar energy. *Renewable and Sustainable Energy Reviews*, **2023**, 183: 113477. https://doi.org/10.1016/j.rser.2023.113477.
[39] Dong, L., Yang, Y., Liu, Z., et al. Effect of chloride ion migration behaviour on the microstructure and mechanical properties of ultra-high performance concrete: A review. *Journal of Building Engineering*, **2024**, 82: 108233. https://doi.org/10.1016/j.jobe.2023.108233.
[40] Sun, J., Jin, Z., Chang, H., et al. A review of chloride transport in concrete exposed to the marine atmosphere zone environment: Experiments and numerical models. *Journal of Building Engineering*, **2024**, 84: 108591. https://doi.org/10.1016/j.jobe.2024.108591.
[41] Yang, J., Zhang, Z., Cheng, Q. Resolution enhancement in micro-XRF using image restoration techniques. *Journal of Analytical Atomic Spectrometry*, **2022**, 37(4): 750–758. https://doi.org/10.1039/d1ja00425e.
[42] Bran-Anleu, P., Wangler, T., Nerella, V. N., et al. Using micro-XRF to characterize chloride ingress through cold joints in 3D printed concrete. *Materials and Structures*, **2023**, 56(3): 51. https://doi.org/10.1617/s11527-023-02132-w.
[43] Sun, H., Qian, J., Yang, Y., et al. Optimization of gypsum and slag contents in blended cement containing slag. *Cement and Concrete Composites*, **2020**, 112: 103674. https://doi.org/10.1016/j.cemconcomp.2020.103674.
[44] Gracioli, B., Angulski da Luz, C., Beutler, C. S., et al. Influence of the calcination temperature of phosphogypsum on the performance of supersulfated cements. *Construction and Building Materials*, **2020**, 262: 119961. https://doi.org/10.1016/j.conbuildmat.2020.119961.
[45] Li, J.S., Zhang, W., Huang, X., et al. MgO-based supersulfated cement with different industrial by-product gypsum: Experiments and molecular dynamics simulation. *Science of the Total Environment*, **2024**, 941: 173756. https://doi.org/10.1016/j.scitotenv.2024.173756.
[46] Dorn, T., Hirsch, T., Stephan, D. Working mechanism of calcium nitrate as an accelerator for Portland cement hydration. *Journal of the American Ceramic Society*, **2023**, 106(1): 752–766. https://doi.org/10.1111/jace.18782.
[47] Xu, L., Sun, Z., Chen, Y., et al. Retardation mechanism of zinc on Portland cement and alite hydration. *Cement and Concrete Research*, **2024**, 184: 107571. https://doi.org/10.1016/j.cemconres.2024.107571.
[48] Zheng, Q., Liang, C., Jiang, J., et al. Alite hydration at the single grain level. *Cement and Concrete Composites*, **2023**, 144: 105297. https://doi.org/10.1016/j.cemconcomp.2023.105297.
[49] Hirsch, T., Matschei, T., Stephan, D. The hydration of tricalcium aluminate ($Ca_3Al_2O_6$) in Portland cement-related systems: A review. *Cement and Concrete Research*, **2023**, 168: 107150. https://doi.org/10.1016/j.cemconres.2023.107150.
[50] Zhu, H., Liao, C., Chen, Z., et al. Role of C-F-S-H/PCE nanocomposites on the hydration of Portland cement with varying gypsum levels. *Construction and Building Materials*, **2024**, 426: 136155. https://doi.org/10.1016/j.conbuildmat.2024.136155.
[51] Aziz, I. H., Al Bakri Abdullah, M. M., Mohd Salleh, M. A. A., et al. Microstructure and porosity evolution of alkali activated slag at various heating temperatures. *Journal of Materials Research and Technology*, **2020**, 9(6): 15894–15907. https://doi.org/10.1016/j.jmrt.2020.11.041.
[52] Wang, J., Gao, C., Tang, J., et al. The multi-scale mechanical properties of calcium-silicate-hydrate. *Cement and Concrete Composites*, **2023**, 140: 105097. https://doi.org/10.1016/j.cemconcomp.2023.105097.
[53] Li, B., Li, Q., Chen, W. Spatial zonation of a hydrotalcite-like phase in the inner product of slag: New insights into the hydration mechanism. *Cement and Concrete Research*, **2021**, 145: 106460. https://doi.org/10.1016/j.cemconres.2021.106460.
[54] Irbe, L., Beddoe, R. E., Heinz, D. The role of aluminium in C-A-S-H during sulfate attack on concrete. *Cement and Concrete Research*, **2019**, 116: 71–80. https://doi.org/10.1016/j.cemconres.2018.11.012.
[55] Kogbara, R. B., Al-Tabbaa, A. Mechanical and leaching behaviour of slag-cement and lime-activated slag stabilised/solidified contaminated soil. *Science of the Total Environment*, **2011**, 409(11): 2325–2335. https://doi.org/10.1016/j.scitotenv.2011.02.037.
[56] He, J., Bai, W., Zheng, W., et al. Influence of hydrated lime on mechanical and shrinkage properties of alkali-activated slag cement. *Construction and Building Materials*, **2021**, 289: 123201. https://doi.org/10.1016/j.conbuildmat.2021.123201.
[57] Boudache, S., Loukili, A., Izoret, L., et al. Investigating the role played by portlandite and C-A-S-H in the degradation response of pozzolanic and slag cements to external sulphate attack.

Journal of Building Engineering, **2023**, 67: 106053. https://doi.org/10.1016/j.jobe.2023.106053.

[58] Kolani, B., Buffo-Lacarrière, L., Sellier, A., et al. Hydration of slag-blended cements. *Cement and Concrete Composites*, **2012**, 34(9): 1009–1018. https://doi.org/10.1016/j.cemconcomp.2012.05.007.

[59] Han, F., Wu, L. Comprehensive utilization of carbide slag. In: *Industrial Solid Waste Recycling in Western China*. Singapore: Springer Singapore, **2019**: 357–391. https://doi.org/10.1007/978-981-13-8086-0_7.

[60] Yi, Y., Zheng, X., Liu, S., et al. Comparison of reactive magnesia- and carbide slag-activated ground granulated blastfurnace slag and Portland cement for stabilisation of a natural soil. *Applied Clay Science*, **2015**, 111: 21–26. https://doi.org/10.1016/j.clay.2015.03.023.

[61] Wang, A., Zhang, C., Sun, W. Fly ash effects: I. The morphological effect of fly ash. *Cement and Concrete Research*, **2003**, 33(12): 2023–2029. https://doi.org/10.1016/S0008-8846(03)00217-5.

[62] Cao, Z., Xia, Y. Study on the preparation and tribological properties of fly ash as lubricant additive for steel/steel pair. *Tribology Letters*, **2017**, 65(3): 104. https://doi.org/10.1007/s11249-017-0885-x.

[63] Ghalehnovi, M., Roshan, N., Hakak, E., et al. Effect of red mud (bauxite residue) as cement replacement on the properties of self-compacting concrete incorporating various fillers. *Journal of Cleaner Production*, **2019**, 240: 118213. https://doi.org/10.1016/j.jclepro.2019.118213.

[64] Romano, R. C. O., Bernardo, H. M., Maciel, M. H., et al. Hydration of Portland cement with red mud as mineral addition. *Journal of Thermal Analysis and Calorimetry*, **2018**, 131(3): 2477–2490. https://doi.org/10.1007/s10973-017-6794-2.

[65] Liu, X., Zhang, N. Utilization of red mud in cement production: A review. *Waste Management & Research: the Journal for a Sustainable Circular Economy*, **2011**, 29(10): 1053–1063. https://doi.org/10.1177/0734242x11407653.

[66] Kang, S. P., Kwon, S. J. Effects of red mud and Alkali-Activated Slag Cement on efflorescence in cement mortar. *Construction and Building Materials*, **2017**, 133: 459–467. https://doi.org/10.1016/j.conbuildmat.2016.12.123.

[67] da Silva Barroso, L., Cherene, M. G. P., de Castro Xavier, G., et al. Bibliometric study of the application of gypsum residues and by-products in Portland cement and mortar. *Construction and Building Materials*, **2023**, 409: 134072. https://doi.org/10.1016/j.conbuildmat.2023.134072.

[68] Chen, J., Jia, J., Zhu, M. Understanding the effect of alkali content on hydration, hardening, and performance of Portland cement–A comprehensive review. *Materials Today Communications*, **2024**, 40: 109728. https://doi.org/10.1016/j.mtcomm.2024.109728.

[69] Li, Y., Zhang, C., Xiang, Y., et al. Microstructure tailoring of internal curing agents: Modified cement particles/superabsorbent polymers composites balancing strength and shrinkage mitigation. *Cement and Concrete Research*, **2025**, 197: 107950. https://doi.org/10.1016/j.cemconres.2025.107950.

[70] Gao, X., Yao, X., Yang, T., et al. Calcium carbide residue as auxiliary activator for one-part sodium carbonate-activated slag cements: Compressive strength, phase assemblage and environmental benefits. *Construction and Building Materials*, **2021**, 308: 125015. https://doi.org/10.1016/j.conbuildmat.2021.125015.

[71] Gong, X., Zhang, T., Zhang, J., et al. Recycling and utilization of calcium carbide slag - current status and new opportunities. *Renewable and Sustainable Energy Reviews*, **2022**, 159: 112133. https://doi.org/10.1016/j.rser.2022.112133.

[72] Wang, H., Xu, W., Sharif, M., et al. Resource utilization of solid waste carbide slag: A brief review of application technologies in various scenes. *Waste Disposal & Sustainable Energy*, **2022**, 4(1): 1–16. https://doi.org/10.1007/s42768-021-00090-z.

[73] Kohno, K., Okamoto, T., Isikawa, Y., et al. Effects of artificial lightweight aggregate on autogenous shrinkage of concrete. *Cement and Concrete Research*, **1999**, 29(4): 611–614. https://doi.org/10.1016/S0008-8846(98)00202-6.

[74] Suntharalingam, S., Takahashi, Y. Experimental study on autogenous shrinkage behaviors of different Portland blast furnace slag cements. *Construction and Building Materials*, **2020**, 230: 116980. https://doi.org/10.1016/j.conbuildmat.2019.116980.

[75] Sirtoli, D., Wyrzykowski, M., Riva, P., et al. Autogenous and drying shrinkage of mortars based on Portland and calcium sulfoaluminate cements. *Materials and Structures*, **2020**, 53(5): 126. https://doi.org/10.1617/s11527-020-01561-1.

[76] Li, Z., Delsaute, B., Lu, T., et al. A comparative study on the mechanical properties, autogenous shrinkage and cracking proneness of alkali-activated concrete and ordinary Portland cement concrete. *Construction and Building Materials*, **2021**, 292: 123418. https://doi.org/10.1016/j.conbuildmat.2021.123418.

[77] Tang, S., Huang, D., He, Z. A review of autogenous shrinkage models of concrete. *Journal of Building Engineering*, **2021**, 44: 103412. https://doi.org/10.1016/j.jobe.2021.103412.

[78] Huang, T. Y., Nguyen, H. A., Chang, T. P., et al. Engineering properties and microstructural performance of low energy supersulfated cement using industrial waste anhydrite. *MATEC Web of Conferences*, **2017**, 130: 04001. https://doi.org/10.1051/matecconf/201713004001.

[79] Feng, Z., Shen, D., Huang, Q., et al. Experimental study on cracking potential and viscoelastic behaviors of supersulfated cement concrete with different compositions. *Journal of Building Engineering*, **2023**, 75: 107023. https://doi.org/10.1016/j.jobe.2023.107023.

[80] Lee, B., Kim, G., Nam, J., et al. Compressive strength, resistance to chloride-ion penetration and freezing/thawing of slag-replaced concrete and cementless slag concrete containing desulfurization slag activator. *Construction and Building Materials*, **2016**, 128: 341–348. https://doi.org/10.1016/j.conbuildmat.2016.10.075.

[81] Maes, M., Gruyaert, E., De Belie, N. Resistance of concrete with blast-furnace slag against chlorides, investigated by comparing chloride profiles after migration and diffusion. *Materials and Structures*, **2013**, 46(1): 89–103. https://doi.org/10.1617/s11527-012-9885-3.

[82] Wu, Q., Xue, Q., Yu, Z. Research status of super sulfate cement. *Journal of Cleaner Production*, **2021**, 294: 126228. https://doi.org/10.1016/j.jclepro.2021.126228.

[83] Whittaker, M., Zajac, M., Ben Haha, M., et al. The impact of alumina availability on sulfate resistance of slag composite cements. *Construction and Building Materials*, **2016**, 119: 356–369. https://doi.org/10.1016/j.conbuildmat.2016.05.015.



Dongmin Wang, PhD in Engineering, is a professor at China University of Mining and Technology-Beijing and the dean of the Institute of Concrete and Environmental Materials. He is also the executive director of the Chinese Ceramic Society, the chairman of the Solid Waste Subcommittee of the Chinese Ceramic Society, and the vice chairman of the RILEM China Branch. He has long been committed to the key research directions of industrial-mining-municipal solid waste resource utilization and low-car-

bon cement concrete material application, solid waste preparation of low-carbon cement and concrete materials, hydraulic lime and ancient building restoration materials, and harmless treatment and resource utilization of municipal waste incineration fly ash. His scientific research results have won 13 provincial and ministerial awards, 55 national invention patents have been authorized, 14 academic monographs have been published, and more than 480 papers have been published in domestic and foreign academic journals.



Huangqi Wang received his PhD degree in June 2024 from China University of Mining and Technology-Beijing, with a focus on the research of concrete admixtures and resource utilization of solid waste.